

Oceanic three-dimensional Lagrangian Coherent Structures: A study of a mesoscale eddy in the Benguela ocean region.

João H. Bettencourt^{1,*}, Cristóbal López, Emilio Hernández-García

*IFISC (CSIC-UIB), Instituto de Física Interdisciplinar y Sistemas Complejos
Campus Universitat de les Illes Balears
E-07122 Palma de Mallorca, Spain*

Abstract

We study three dimensional oceanic Lagrangian Coherent Structures (LCSs) in the Benguela region, as obtained from an output of the ROMS model. To do that we first compute Finite-Size Lyapunov exponent (FSLE) fields in the region volume, characterizing mesoscale stirring and mixing. Average FSLE values show a general decreasing trend with depth, but there is a local maximum at about 100 m depth. LCSs are extracted as ridges of the calculated FSLE fields. They present a “curtain-like” geometry in which the strongest attracting and repelling structures appear as quasivertical surfaces. LCSs around a particular cyclonic eddy, pinched off from the upwelling front are also calculated. The LCSs are confirmed to provide pathways and barriers to transport in and out of the eddy.

Keywords: Lagrangian Coherent Structures, Finite-Size Lyapunov exponents, ocean transport, Benguela upwelling region, oceanic eddy

1. Introduction.

Mixing and transport processes are fundamental to determine the physical, chemical and biological properties of the oceans. From plankton dynamics to the evolution of pollutant spills, there is a wide range of practical issues that benefit from a correct understanding and modeling of these processes. Although mixing and transport in the oceans occur in a wide range of scales, mesoscale and sub-mesoscale variability are known to play a very important role (Thomas et al., 2008; Klein and Lapeyre, 2009).

Mesoscale eddies are especially important in this aspect because of their long life in oceanic flows, and their stirring and mixing properties. In the southern Benguela, for instance, cyclonic eddies shed from the Agulhas current can transport and exchange warm waters from the Indian Ocean to the South Atlantic (Byrne et al., 1995; Lehahn et al., 2011). Moreover, mesoscale eddies have been shown to drive important biogeochemical processes in the ocean such as the vertical flux of nutrients into the euphotic zone (McGillicuddy et al., 1998; Oschlies and Garçon, 1998). Another effect of eddy activity seems to be the intensification of mesoscale and sub-mesoscale variability due to the filamentation process where strong tracer gradients are created by the stretching of tracers in the shear- and strain-dominated regions in between eddy cores (Elhmaïdi et al., 1993). Studies of the vertical structure of such eddies in the Benguela region (e. g. Doglioli et al. (2007) and Rubio

et al. (2009)) have shown that they can extended to one thousand meters deep waters.

In the last decades new developments in the description and modelling of oceanic mixing and transport from a Lagrangian viewpoint have emerged (Mariano et al., 2002; Lacasce, 2008). These Lagrangian approaches have become more and more frequent due to the increased availability of detailed knowledge of the velocity field from Lagrangian drifters, satellite measurements and computer models. In particular, the very relevant concept of Lagrangian Coherent Structure (LCS) (Haller, 2000; Haller and Yuan, 2000) is becoming crucial for the analysis of transport in flows. LCSs are structures that separate regions of the flow with different dynamical behavior. They give a general geometric view of the dynamics, acting as a (time-dependent) roadmap for the flow. They are templates serving as proxies to, for instance, barriers and avenues to transport or eddy boundaries (Boffetta et al., 2001; Haller and Yuan, 2000; Haller, 2002; d’Ovidio et al., 2004, 2009; Mancho et al., 2006).

The relevance of the three-dimensional structure of LCSs begins to be unveiled in atmospheric contexts (du Toit and Marsden, 2010; Tang et al., 2011; Tallapragada et al., 2011). In the case of oceanic flows, however, the identification of the LCSs and the study of their role on biogeochemical tracers transport has been mostly restricted to the marine surface (d’Ovidio et al., 2004; Waugh et al., 2006; d’Ovidio et al., 2009; Beron-Vera et al., 2008). This is mainly due to two reasons: a) tracer vertical displacement is usually very small with respect to the horizontal one; and b) satellite data of any quantity (temperature, chlorophyll, altimetry for velocity, etc..) are only available from the observation of the ocean surface.

*Corresponding author

Email address: joaob@ifisc.uib-csic.es (João H. Bettencourt)

¹Phone: +34 971259905

Oceanic flows can be considered mainly two-dimensional, because there is a great disparity between the horizontal and vertical length scales, and they are strongly stratified due to the Earth's rotation. There are, however, areas in the ocean where vertical motions are fundamental. Firstly there are the so-called upwelling regions, which are the most biologically active marine zones in the world (Rossi et al., 2008; Pauly and Christensen, 1995). The reason is that due to an Ekman pumping mechanism close to the coast, there is a surface uprising of deep cold waters rich in nutrients, inducing a high proliferation of plankton concentration. Typically, vertical velocities in upwelling regions are much larger than in open ocean, but still one order of magnitude smaller than horizontal velocities. Another example where there are significant vertical processes are mesoscale eddies producing submesoscale structures (frontogenesis), which are responsible for strong ageostrophic vertical process, in addition to the vertical exchange thought to occur at the eddy interior (Klein and Lapeyre, 2009). Thus, the identification of the three-dimensional (3d) LCSs in these areas is crucial, as well as understanding their correlations with biological activity. Another reason to include the third dimension in LCS studies is to investigate the vertical variation in their properties.

The main objective of this paper is the characterization of 3d LCSs, extracted in an upwelling region, the Benguela area in the Southern Atlantic Ocean. For this goal we use Finite-Size Lyapunov Exponents (FSLEs). FSLEs (Aurell et al., 1997; Artale et al., 1997) measure the separation rate of fluid particles between two given distance thresholds. LCSs are computed as the ridges of the FSLE field (d'Ovidio et al., 2004; Molcard et al., 2006; Haza et al., 2008; d'Ovidio et al., 2009; Poje et al., 2010; Haza et al., 2010). The rigorous definition of LCS as ridges of a Lagrangian stretching measure was given for the Finite-Time Lyapunov Exponents (FTLE) in Shadden et al. (2005) and Lekien et al. (2007), which are closely related to FSLEs. More recently, hyperbolic LCS have been defined independently of such stretching measures by Haller (2011). Following many previous studies (d'Ovidio et al., 2004; Molcard et al., 2006; d'Ovidio et al., 2009; Branicki and Wiggins, 2009) we adopt the mathematical results for Finite-Time Lyapunov Exponents (FTLE) to FSLE, assuming them to be valid. In particular, we assume that LCS are identified with ridges (Haller, 2001), i.e., the local extrema of the FTLE field, and also we expect, in accordance to the results in Shadden et al. (2005) and Lekien et al. (2007) for FTLEs, that the material flux through these LCS is small and that they are transported by the flow as quasi-material surfaces.

To confirm that our identification of LCSs with ridges of the FSLE field, we perform (in Sect. III) direct particle trajectory integrations that show that the computed LCS really organize the tracer flow. In our work, we will emphasize the numerical methodology since up to now FSLEs have only been computed for the marine surface (an exception is Özgökmen et al. (2011)). We then focus on a particular eddy very prominent in the area at the chosen temporal window and study the stirring and mixing on it's vicinity. Some previous results for Lagrangian eddies were obtained by Branicki and Kirwan (2010) and Branicki

et al. (2011), applying the methodology of lobe dynamics and the turnstile mechanism to eddies pinched off from the Loop Current. In this paper we focus on FSLE fields and the associated particle trajectories to study transport in and out of the chosen mesoscale eddy. Since this is a first attempt to study 3d oceanic LCS, more general results (on Benguela and other upwelling regions) are left for future work.

To circumvent the lack of appropriate observational data in the vertical direction, we use velocity fields from a numerical simulation. They are high resolution simulations from the ROMS model (see section 2 below) thus appropriate to study regional-medium scale basins.

The paper is organized as follows: In section II we describe the data and methods. In section III we present our results. Section IV contains a discussion of the results and Section V summarizes our conclusions.

2. Data and Methods.

2.1. Velocity data set.

The Benguela ocean region is situated off the west coast of southern Africa. It is characterized by a vigorous coastal upwelling regime forced by equatorward winds, a substantial mesoscale activity of the upwelling front in the form of eddies and filaments, and also by the northward drift of Agulhas eddies.

The velocity data set comes from a regional ocean model simulation of the Benguela Region (Le Vu et al., 2011). ROMS (Shchepetkin and McWilliams, 2003, 2005) is a split-explicit free-surface, topography following model. It solves the incompressible primitive equations using the Boussinesq and hydrostatic approximations. Potential temperature and salinity transport are included by coupling advection/diffusion schemes for these variables. The model was forced with climatological data. The data set area extends from 12°S to 35°S and from 4°E to 19°E (see Fig. 1). The velocity field $\mathbf{u} = (u, v, w)$ consists of two years of daily averaged zonal (u), meridional (v), and vertical velocity (w) components, stored in a three-dimensional grid with an horizontal resolution of 1/12 degrees \sim 8 km, and 32 vertical terrain-following levels using a stretched vertical coordinate where the layer thickness varies, increasing from the surface to the ocean interior. Since the ROMS model considers the hydrostatic approximation it is important to note that Mahadevan (2006), when comparing results from non-hydrostatic and hydrostatic versions of the same model of vertical motions at submesoscale fronts, found that while instantaneous vertical velocities structures differ, the averaged vertical flux is similar in both hydrostatic and non-hydrostatic simulations.

2.2. Finite-Size Lyapunov Exponents.

In order to study non-asymptotic dispersion processes such as stretching at finite scales and time intervals, the Finite Size Lyapunov Exponent (Aurell et al., 1997; Artale et al., 1997) is particularly well suited. It is defined as:

$$\lambda = \frac{1}{\tau} \log \frac{\delta_f}{\delta_0}, \quad (1)$$

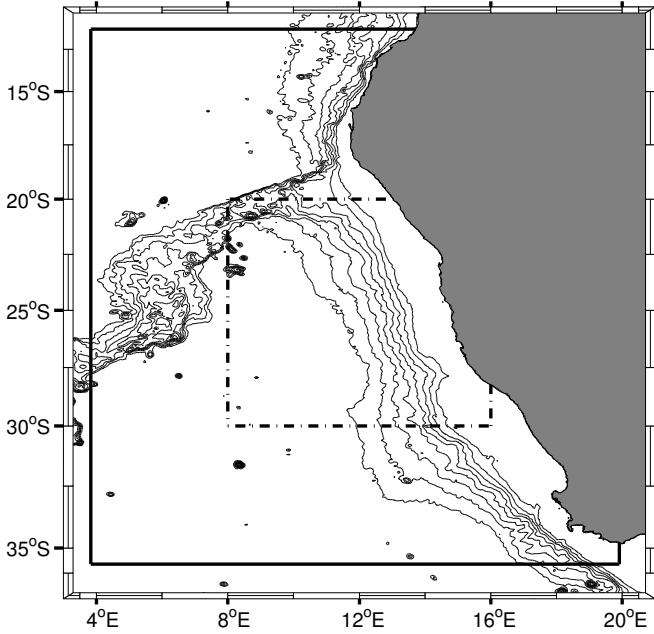


Figure 1: Benguela ocean region. The velocity field domain is limited by the continuous black line. The FSLE calculation area is limited by the dash-dot black line. Bathymetric contour lines are from ETOPO1 global relief model (Amante and Eakins, 2009) starting a 0 m depth up to 4000 m at 500 m interval.

166 where τ is the time it takes for the separation between two particles, initially δ_0 , to reach δ_f . In addition to the dependence
 167 on the values of δ_0 and δ_f , the FSLE depends also on the initial
 168 position of the particles and on the time of deployment. Locations (i.e. initial positions) leading to high values of this
 169 Lyapunov field identify regions of strong separation between particles, i.e., regions that will exhibit strong stretching during
 170 evolution, that can be identified with the LCS (Boffetta et al., 2001; d’Ovidio et al., 2004; Joseph and Legras, 2002).

175 In principle, for computing FSLEs in three dimensions one
 176 just needs to extend the method of d’Ovidio et al. (2004), that is,
 177 one needs to compute the time that fluid particles initially separated by $\delta_0 = [(\delta x_0)^2 + (\delta y_0)^2 + (\delta z_0)^2]^{1/2}$ need to reach a final
 178 distance of $\delta_f = [(\delta x_f)^2 + (\delta y_f)^2 + (\delta z_f)^2]^{1/2}$. The main difficulty
 179 in doing this is that in the ocean vertical displacements (even in
 180 upwelling regions) are much smaller than the horizontal ones,
 181 and so do not contribute significantly to total particle dispersion
 182 (Özgökmen et al., 2011). By the time the horizontal particle dispersion
 183 has scales of tenths or hundreds of kilometers (typical mesoscale structures are studied using $\delta_f \approx 100\text{km}$ (d’Ovidio
 184 et al., 2004)), particle dispersion in the vertical can have at most
 185 scales of hundreds of meters and usually less. This means that
 186 the vertical separation will not contribute significantly to the accumulated distance between particles. In addition, since length
 187 scales in the horizontal and vertical differ by several orders of
 188 magnitude, one faces the impossibility of assigning equal δ_0
 189 to the horizontal and vertical particle pairs. It should be noted
 190 however that these shortcomings arise from the different scales
 191 of length and time that characterize horizontal and vertical dispersion processes in the ocean, and so should not be seen as
 192 intrinsic limitations of the method. For non-oceanic flows a di-

197 rect generalization of FSLEs is straightforward.

198 Thus, in this paper we implemented a quasi three-dimensional computation of FSLEs. That is, we make the computation for every (2d) ocean layer, but where the particle trajectories calculation use the full 3d velocity field. I.e., at each level (depth) we set $\delta z_0 = 0$, and the final distance is computed without taking the vertical distance between particles. It is important to note that, since we allow the particles to evolve in the full 3d velocity field, we take into account vertical quantities such as vertical velocity shear that may influence the horizontal separation between particle pairs.

208 There are other possible approaches to the issue of different scales in the vertical and horizontal. One way is to assign anisotropic initial and final displacements in the FSLE calculation (i. e., including a δz_0 and δz_f much smaller than the horizontal initial and final separations). A second approach is to use different weights for the horizontal and vertical separations in the calculations of the distance, perhaps in combination with the first. We have checked both alternatives and found that, with reasonable choices of initial and final distances and distance metrics, the results were equivalent to the quasi-3d computation. The reason is that actual dispersion is primarily horizontal as commented above.

220 More in detail, a grid of initial locations \mathbf{x}_0 in the longitude/latitude/depth geographical space (ϕ, θ, z) , fixing the spatial resolution of the FSLE field, is set up at time t . The horizontal distance among the grid points, δ_0 , was set to $1/36$ degrees (≈ 3 km), i.e. three times finer resolution than the velocity field (Hernandez-Carrasco et al., 2011), and the vertical resolution (distance between layers) was set to 20 m in order to have a good representation of the vertical variations in the FSLE field. Particles are released from each grid point and their three dimensional trajectories calculated. The distances of each particle with respect to the ones that were initially neighbors at an horizontal distance δ_0 are monitored until one of the horizontal separations reaches a value δ_f . By integrating the three dimensional particle trajectories backward and forward in time, we obtain the two different types of FSLE maps: the attracting LCS (for the backward), and the repelling LCS (forward) (d’Ovidio et al., 2004; Joseph and Legras, 2002). We obtain in this way FSLE fields with a horizontal spatial resolution given by δ_0 . The final distance δ_f was set to 100 km, which is, as already mentioned, a typical length scale for mesoscale studies. The trajectories were integrated for a maximum of $T = 178$ days (approximately six months) using an integration time step of 6 hours. When a particle reached the coast or left the velocity field domain, the FSLE value at its initial position and initial time was set to zero. If the interparticle horizontal separation remains smaller than δ_f during all the integration time, then the FSLE for that location is also set to zero.

247 The equations of motion that describe the evolution of parti-

248 cle trajectories are

$$249 \quad \frac{d\phi}{dt} = \frac{1}{R_z} \frac{u(\phi, \theta, z, t)}{\cos(\theta)}, \quad (2)$$

$$250 \quad \frac{d\theta}{dt} = \frac{1}{R_z} v(\phi, \theta, z, t), \quad (3)$$

$$251 \quad \frac{dz}{dt} = w(\phi, \theta, z, t), \quad (4)$$

252 where ϕ is longitude, θ is latitude and z is the depth. R_z is the
 253 radial coordinate of the moving particle $R_z = R - z$, with $R =$
 254 6371 km the mean Earth radius. For all practical purposes, $R_z \approx$
 255 R . Particle trajectories are integrated using a 4th order Runge-
 256 Kutta method. For the calculations, one needs the (3d) velocity
 257 values at the current location of the particle. Since the six grid
 258 nodes surrounding the particle do not form a regular cube, direct
 259 trilinear interpolation can not be used. Thus, an isoparametric
 260 element formulation is used to map the nodes of the velocity
 261 grid surrounding the particles position to a regular cube, and
 262 an inverse isoparametric mapping scheme (Yuan et al., 1994)
 263 is used to find the coordinates of the interpolation point in the
 264 regular cube coordinate system.

265 2.3. Lagrangian Coherent Structures.

266 In 2d, LCS practically coincide with (finite-time) stable and
 267 unstable manifolds of relevant hyperbolic structures in the flow
 268 (Haller, 2000; Haller and Yuan, 2000; Joseph and Legras, 2002).
 269 The structure of these last objects in 3d is generally
 270 much more complex than in 2d (Haller, 2001; Pouransari et al.,
 271 2010), and they can be locally either lines or surfaces. As com-
 272 mented before, however, vertical motions in the ocean are slow.
 273 Thus, at each fluid parcel the strongest attracting and repelling
 274 directions should be nearly horizontal. This, combined with
 275 the incompressibility property, implies that the most attracting
 276 and repelling regions (i.e. the LCSs) should appear as almost
 277 vertical surfaces, since the attraction or repulsion should occur
 278 normally to the LCS. As a consequence, the LCSs will have a
 279 ‘‘curtain-like’’ geometry, with deviations from the vertical due
 280 to either the orientation of the most attracting or repelling direc-
 281 tion deviating from the horizontal, or when strong vertical shear
 282 produces variations along the vertical in the most repelling or
 283 attracting regions in the flow. We expect the LCS sheet-like ob-
 284 jects to coincide with the strongest hyperbolic manifolds when
 285 these are two dimensional, and to contain the strongest hyper-
 286 bolic lines.

287 The curtain-like geometry of the LCS was already com-
 288 mented in Branicki and Malek-Madani (2010), Branicki and
 289 Kirwan (2010), or Branicki et al. (2011). In the latter paper
 290 it was shown that, in a 3d flow, these structures would appear
 291 mostly vertical when the ratio of vertical shear of the horizon-
 292 tal velocity components to the average horizontal velocities is
 293 small. This ratio also determines the vertical extension of the
 294 structures. In Branicki and Kirwan (2010), the argument was
 295 used to construct a 3d picture of hyperbolic structures from the
 296 computation in a 2d slice. In the present paper we confirm the
 297 curtain-like geometry of the LCSs, and show that they are rele-
 298 vant to organize the fluid flow in this realistic 3d oceanic setting.

299 This is done in the next section by comparing actual particle tra-
 300 jectories with the computed LCSs.

301 Differently than 2d, where LCS can be visually identified as
 302 the maxima of the FSLE field, in 3d the ridges are hidden within
 303 the volume data. Thus, one needs to explicitly compute and
 304 extract them, using the definition of LCSs as the ridges of the
 305 FSLEs. A ridge L is a co-dimension 1 orientable, differentiable
 306 manifold (which means that for a three-dimensional domain D ,
 307 ridges are surfaces) satisfying the following conditions (Lekien
 308 et al., 2007):

- 309 1. The field λ attains a local extremum at L .
- 310 2. The direction perpendicular to the ridge is the direction of
 311 fastest descent of λ at L .

312 Mathematically, the two previous requirements can be ex-
 313 pressed as

$$314 \quad \mathbf{n}^T \nabla \lambda = 0, \quad (5)$$

$$315 \quad \mathbf{n}^T \mathbf{H} \mathbf{n} = \min_{\|\mathbf{u}\|=1} \mathbf{u}^T \mathbf{H} \mathbf{u} < 0, \quad (6)$$

316 where $\nabla \lambda$ is the gradient of the FSLE field λ , \mathbf{n} is the unit nor-
 317 mal vector to L and \mathbf{H} is the Hessian matrix of λ .

318 The method used to extract the ridges from the scalar field
 319 $\lambda(\mathbf{x}_0, t)$ is from Schultz et al. (2010). It uses an earlier (Eberly
 320 et al., 1994) definition of ridge in the context of image analy-
 321 sis, as a generalized local maxima of scalar fields. For a scalar
 322 field $f : \mathbb{R}^n \rightarrow \mathbb{R}$ with gradient $\mathbf{g} = \nabla f$ and Hessian \mathbf{H} , a
 323 d -dimensional height ridge is given by the conditions

$$324 \quad \forall_{d < i \leq n} \mathbf{g}^T \mathbf{e}_i = 0 \text{ and } \alpha_i < 0, \quad (7)$$

325 where $\alpha_i, i \in \{1, 2, \dots, n\}$, are the eigenvalues of \mathbf{H} , ordered
 326 such that $\alpha_1 \geq \dots \geq \alpha_n$, and \mathbf{e}_i is the eigenvector of \mathbf{H} associ-
 327 ated with α_i . For $n = 3$, (7) becomes

$$328 \quad \mathbf{g}^T \mathbf{e}_3 = 0 \text{ and } \alpha_3 < 0. \quad (8)$$

329 This ridge definition is equivalent to the one given by (5) since
 330 the unit normal \mathbf{n} is the eigenvector (when normalized) associ-
 331 ated with the minimum eigenvalue of \mathbf{H} . In other words, in \mathbb{R}^3
 332 the $\mathbf{e}_1, \mathbf{e}_2$ eigenvectors point locally along the ridge and the \mathbf{e}_3
 333 eigenvector is orthogonal to it.

334 The ridges extracted from the backward FSLE map approxi-
 335 mate the attracting LCS, and the ridges extracted from the for-
 336 ward FSLE map approximate the repelling LCS. The attract-
 337 ing ones are the more interesting from a physical point of view
 338 (d’Ovidio et al., 2004, 2009), since particles (or any passive
 339 scalar driven by the flow) typically approach them and spread
 340 along them, giving rise to filament formation. In the extrac-
 341 tion process it is necessary to specify a threshold s for the ridge
 342 strength $|\alpha_3|$, so that ridge points whose value of α_3 is lower
 343 (in absolute value) than s are discarded from the extraction pro-
 344 cess. Since the ridges are constructed by triangulations of the
 345 set of extracted ridge points, the s threshold greatly determines
 346 the size and shape of the extracted ridge, by filtering out re-
 347 gions of the ridge that have low strength. The reader is referred
 348 to Schultz et al. (2010) for details about the ridge extraction
 349 method. The height ridge definition has been used to extract
 350 LCS from FTLE fields in several works (see, among others,
 351 Sadlo and Peikert (2007)).

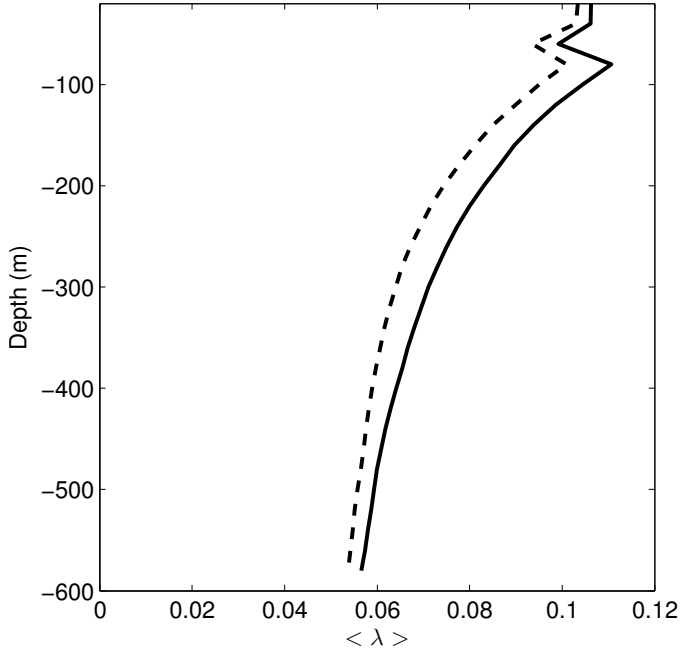


Figure 2: Vertical profile of 30 day average backward and forward FSLE. The 30 day average field was spatially averaged at each layer over the FSLE calculation area to produce the vertical profiles. The backward FSLE average is shown in continuous and the forward FSLE is shown in dashed.

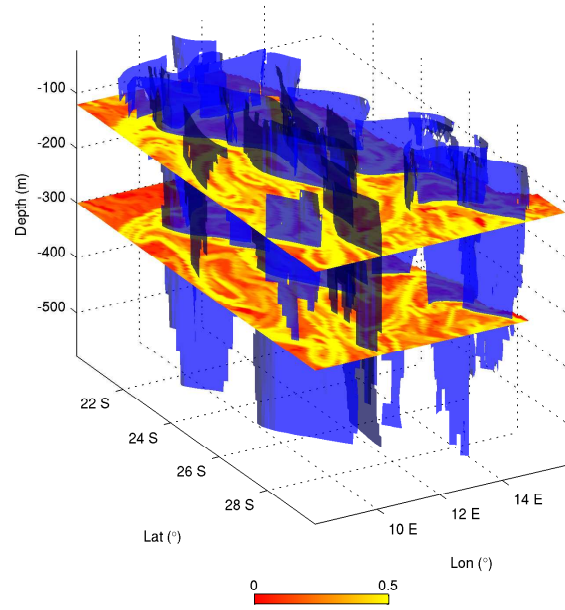


Figure 3: Attracting LCS (blue) for day 1 of the calculation period, together with horizontal slices of the backward FSLE field at 120 m and 300 m depth. Colorbar refers to colormap of horizontal slices. The units of the colorbar are day^{-1} .

3. Results

3.1. Three dimensional FSLE field

The three dimensional FSLE field was calculated for a 30 day period starting September 17, with snapshots taken every 2 days. The fields were calculated for an area of the Benguela ocean region between latitudes $20^{\circ}S$ and $30^{\circ}S$ and longitudes $8^{\circ}E$ to $16^{\circ}E$ (see figure 1). The area is bounded at NW by the Walvis Ridge and the continental slope approximately bisects the region from NW to SE. The western half of the domain has abyssal depths of about 4000 m. The calculation domain extended vertically from 20 up to 580 m of depth. Both backward and forward calculations were made in order to extract the attracting and repelling LCS.

Figure 2 displays the vertical profile of the average FSLE for the 30 day period. There are small differences between the backward and the forward values due to the different intervals of time involved in their calculation. But both profiles have a similar shape and show a general decrease with depth. There is a notable peak in the profiles at about 100 m depth that indicates increased mesoscale variability (and transport, as shown in Sect. 3.2 at that depth).

A snapshot of the attracting LCSs for day 1 of the calculation period is shown in figure 3. As expected, the structures appear as thin vertical curtains, most of them extending throughout the depth of the calculation domain. The area is populated with LCS, denoting the intense mesoscale activity in the Benguela region. As already mentioned, in three dimensions the ridges are not easily seen, since they are hidden in the volume data. However the horizontal slices of the field in figure 3 show that the attracting LCS fall on the maximum backward FSLE field

lines of the 2d slices. The repelling LCS (not shown) also fall on the maximum forward FSLE field lines of the 2d slices.

Since the λ value of a point on the ridge and the ridges strength α_3 are only related through the expressions (7) and (8), the relationship between the two quantities is not direct. This creates a difficulty in choosing the appropriate strength threshold for the extraction process. A too small value of s will result in very small LCS that appear to have little influence on the dynamics, while a greater value will result in only a partial rendering of the LCS, limiting the possibility of observing their real impact on the flow. Computations with several values of s lead us to the optimum choice $s = 20 \text{ day}^{-1}m^{-2}$, meaning that grid nodes with $\alpha_3 < -20 \text{ day}^{-1}m^{-2}$ were filtered out from the LCS triangulation.

We have seen in this section an example of how the ridges of the 3d FSLE field, the LCS, distribute in the Benguela ocean region. Their ubiquity shows their impact on the transport and mixing properties. In the next section we concentrate on the properties of a single 3d mesoscale eddy.

3.2. Study of the dynamics of a relevant mesoscale eddy

Let us study a prominent cyclonic eddy observed in the data set. The trajectory of the center of the eddy was tracked and it is shown in figure 4. The eddy was apparently pinched off at the upwelling front. At day 1 of the FSLE calculation period its center was located at latitude $24.8^{\circ}S$ and longitude $10.6^{\circ}E$, leaving the continental slope, and having a diameter of approximately 100 km. One may ask: what is its vertical size? is it really a barrier, at any depth, for particle transport?

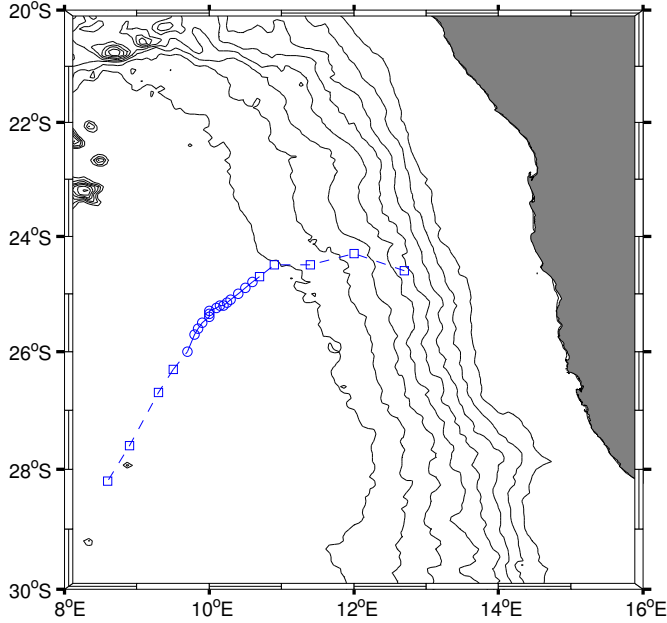


Figure 4: Trajectory (advancing from NE to SW) of the eddy center inside the calculation domain. Circles indicate the center location during the 30 day FSLE calculation period, and squares previous and posterior positions. Bathymetric lines same as in figure 1.

To properly answer these questions the eddy, in particular its frontiers, should be located. From the Eulerian point of view it is commonly accepted that eddies are delimited by closed contours of vorticity and that the existence of strong vorticity gradients prevent the transport in and out of the eddy. Such transport may occur when the eddy is destroyed or undergoes strong interactions with other eddies (Provenzale, 1999). In a Lagrangian view point, however, an eddy can be defined as a region delimited by intersections and tangencies of LCS, whether in 2d or 3d space. The eddy itself is an elliptic structure (Haller and Yuan, 2000; Branicki and Kirwan, 2010; Branicki et al., 2011). In this Lagrangian view of an eddy, the transport inhibition to and from the eddy is now related to the existence of these transport barriers delimiting the eddy region, which are known to be quasi impermeable.

Using the first approach, i.e., the Eulerian view, the vertical distribution of the Q -criteria (Hunt et al., 1988; Jeong and Hussain, 1995) was used to determine the vertical extension of the mesoscale eddy. The Q criterium is a 3d version of the Okubo-Weiss criterium (Okubo, 1970; Weiss, 1991) and measures the relative strength of vorticity and straining. In this context, eddies are defined as regions with positive Q , with Q the second invariant of the velocity gradient tensor

$$Q = \frac{1}{2} (\|\boldsymbol{\Omega}\|^2 - \|\mathbf{S}\|^2), \quad (9)$$

where $\|\boldsymbol{\Omega}\|^2 = \text{tr}(\boldsymbol{\Omega}\boldsymbol{\Omega}^T)$, $\|\mathbf{S}\|^2 = \text{tr}(\mathbf{S}\mathbf{S}^T)$ and $\boldsymbol{\Omega}$, \mathbf{S} are the anti-symmetric and symmetric components of $\nabla\mathbf{u}$. Using $Q = 0$ as the Eulerian eddy boundary, it can be seen from Fig. 5 that the eddy extends vertically down to, at least, 600 m.

Let us move to the Lagrangian description of eddies, which is much in the spirit of our study, and will allow us to study

particle transport: eddies can be defined as the *region bounded by intersecting or tangent repelling and attracting LCS* (Branicki and Kirwan, 2010; Branicki et al., 2011). Using this criterion, and first looking at the surface located at 200 m depth, we see in Fig. 6 that certainly the Eulerian eddy seems to be located inside the area defined by several intersections and tangencies of the LCS. This eddy has an approximate diameter of 100 km. In the south-north direction there are two intersections that appear to be hyperbolic points (H1 and H2 in figure 6). In the West-East direction, the eddy is closed by a tangency at the western boundary, and a intersection of lines at the eastern boundary. The eddy core is devoid of high FSLE lines, indicating that weak stirring occurs inside (d’Ovidio et al., 2004). As additional Eulerian properties, we note that near or at the intersections H1 and H2 the Q -criterium indicates straining motions. In the case of H2, figure 5 (right panel) indicates high shear up to 200 m depth. The fact that the hyperbolic regions H1 and H2 lie in strain dominated regions of the flow ($Q < 0$) highlights the connection between hyperbolic particle behavior and instantaneous hyperbolic regions of the flow. The ridges of the FSLE field, however, do not remain in the negative Q regions but cross into rotation dominated regions with $Q > 0$. This indicates that there are some differences between the Eulerian view (Q) and the Lagrangian view (FSLE). It is the latter that can be understood in terms of particle behaviour as limiting regions of initial conditions (particles) that stay away from hyperbolic regions for long enough time (Haller and Yuan, 2000).

In 3d, the eddy is also surrounded by a set of attracting and repelling LCS (figure 7), calculated as explained in Subsection 2.3. The lines identified in figure 6 are now seen to belong to the vertical of these surfaces.

Note that the vertical extent of these surfaces is in part determined by the strength parameter used in the LCS extraction process, so their true vertical extension is not clear from the results presented here. On the south, the closure of the Lagrangian eddy boundary extends down to the maximum depth of the calculation domain, but moving northward it is seen that the LCS shorten their depth. Probably this does not mean that the eddy is shallower in the North, but rather that the LCS are losing strength (lower $|\alpha_3|$) and portions of it are filtered out by the extraction process. In any case, it is seen that as in two-dimensional calculations, the LCS delimiting the eddy do not perfectly coincide with its Eulerian boundary (Joseph and Legras, 2002), and we expect the Lagrangian view to be more relevant to address transport questions.

In the next paragraphs we analyze the fluid transport across the eddy boundary. Some previous results for Lagrangian eddies were obtained by Branicki and Kirwan (2010) and Branicki et al. (2011). Applying the methodology of lobe dynamics and the turnstile mechanism to eddies pinched off from the Loop Current, Branicki and Kirwan (2010) observed a net fluid entrainment near the base of the eddy, and net detrainment near the surface, being fluid transport in and out of the eddy essentially confined to the boundary region. Let us see what happens in our setting.

We consider six sets of 1000 particles each, that were released at day 1 of the FSLE calculation period, and their trajec-

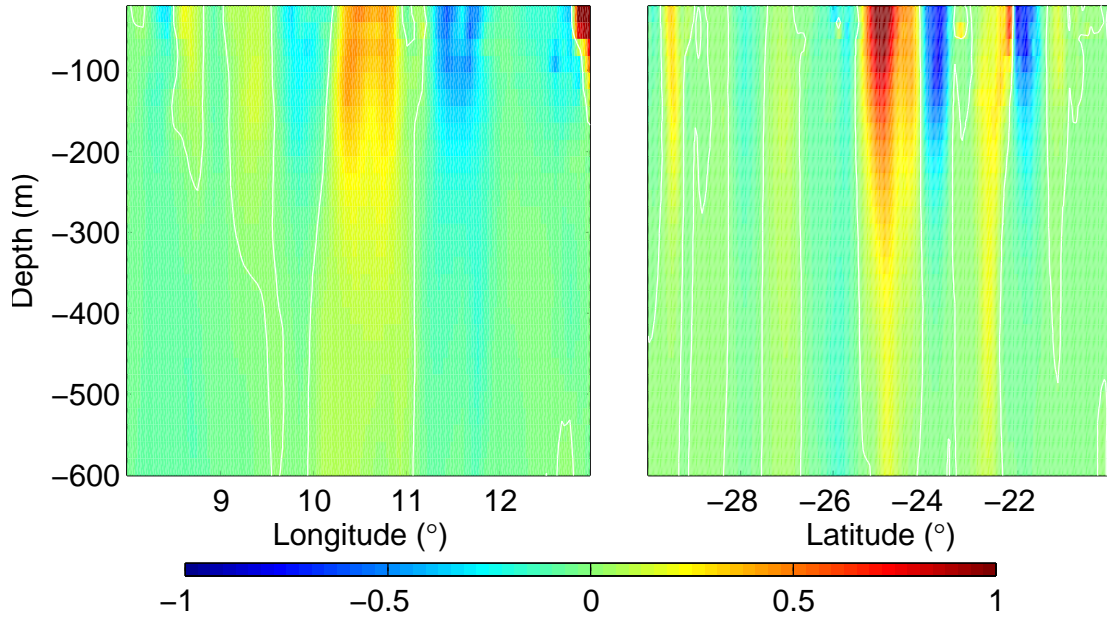


Figure 5: Colormap of Q -criterion. White contours have $Q = 0$. Day 1 of the 30 day FSLE calculation period. Left panel: Latitude 24.5°S ; Right panel: Longitude 10.5°E . Colorbar values are $Q \times 10^{10} \text{ s}^{-2}$.

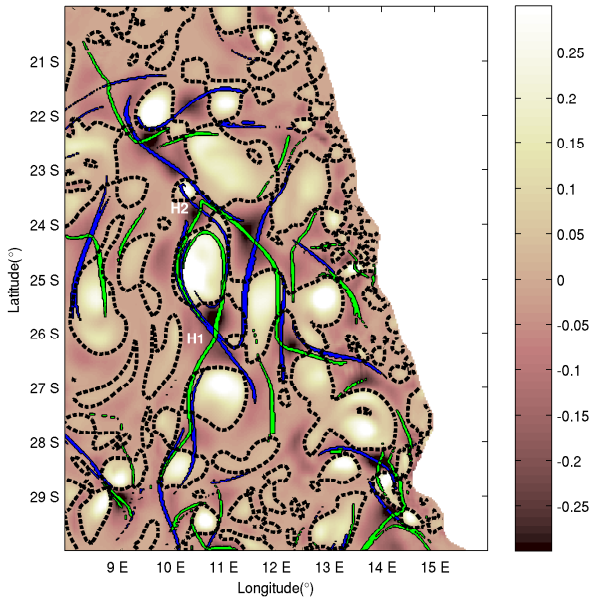


Figure 6: Q -criterion map at 200 m depth together with patches of backward (blue) and forward (green) FSLE values. Black dashed lines have $Q = 0$. FSLE patches contain the highest 60% of FSLE values. Colorbar values are $Q \times 10^{10} \text{ s}^{-2}$. The eddy we study is the clear region in between points H1 and H2.

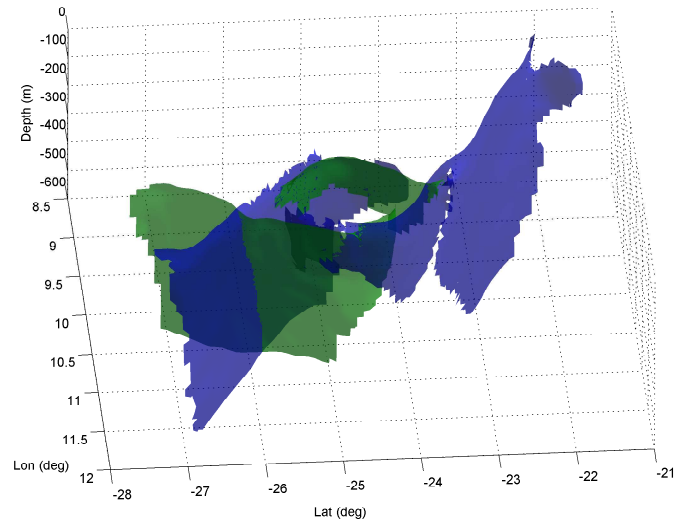


Figure 7: 3d LCSs around the mesoscale eddy at day 1 of the 30 day FSLE calculation period. Green: repelling LCS; Blue: attracting LCS.

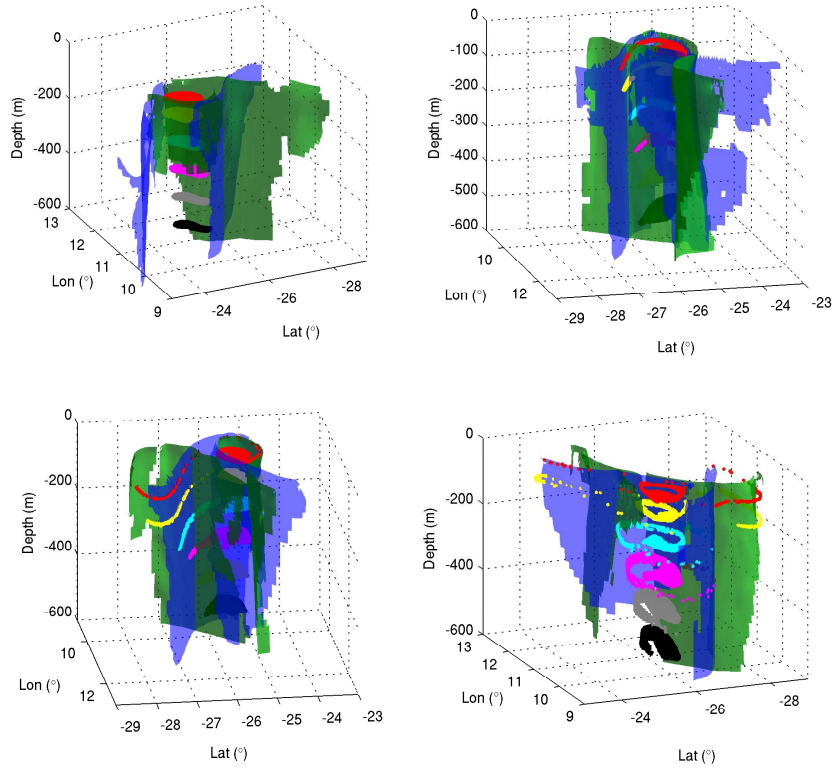


Figure 8: Three dimensional view of the evolution of elliptic patches released at different depths inside of the eddy at day 1 of the 30 day FSLE calculation period. Top left: day 3; Top right: day 13; Bottom left: day 19; Bottom right: day 29. Red: 40 m; Yellow: 100 m; Cyan: 200 m; Magenta: 300 m; Grey: 400 m; Black: 500 m. Attracting LCS are shaded in blue while repelling LCS are shaded in green.

497 tories integrated by a fourth-order Runge-Kutta method with a 521
 498 integration time step of 6 hours. The sets of particles were 522
 499 released at depths of 50, 100, 200, 300, 400 and 500 m. In figure 523
 500 8 we plot the particle sets together with the Lagrangian bound- 524
 501 aries of the mesoscale eddy viewed in 3d. A top view is shown 525
 502 in figure 9. As expected, vertical displacements are small. 526

503 At day 3 (top left panel of figures 8 and 9) it can be seen that 527
 504 there is a differential rotation (generally cyclonic, i.e. clock- 528
 505 wise) between the sets of particles at different depths. The shall- 529
 506 ower sets rotate faster than the deeper ones. This differential 530
 507 rotation of the fluid particles could be viewed, in a Lagrangian 531
 508 perspective, as the fact that the attracting and repelling strength 532
 509 of the LCS that limit the eddy varies with depth. Note that the 533
 510 six sets of particles are released at the same time and at the same 534
 511 horizontal positions, and thereby their different behavior is due 535
 512 to the variations of the LCS properties along depth. 536

513 At day 13 the vortex starts to expel material through filament- 537
 514 ation (Figs.8 and 9, top right panels). A fraction of the parti- 538
 515 cles approach the southern boundaries of the eddy from the 539
 516 northeast. Those to the west of the repelling LCS (green) turn 540
 517 west and recirculate inside the eddy along the southern attract- 541
 518 ing LCS (blue). Particles to the east of the repelling LCS turn 542
 519 east and leave the eddy forming a filament aligned with an attract- 543
 520 ing (blue) LCS. At longer times trajectories in the south of 544

the eddy are influenced by additional structures associated to 521
 a different southern eddy. At day 29 (bottom right panels) the 522
 same process is seen to have occurred in the northern bound- 523
 ary, with a filament of particles leaving the eddy along the north- 524
 ern attracting (blue) LCS. The filamentation seems to begin ear- 525
 lier at shallower waters than at deeper ones since the length of the 526
 expelled filament diminishes with depth. However all of the 527
 expelled filaments follow the same attracting LCS. Figure 10 528
 shows the stages previous to filamentation in which the LCS 529
 structure, their tangencies and crossings, and the paths of the 530
 particle patches are more clearly seen. Note that the LCS do not 531
 form fully closed structures and the particles escape the eddy 532
 through their openings. The images suggest lobe-dynamics pro- 533
 cesses, but much higher precision in the LCS extraction would 534
 be needed to really see such details. 535

536 This filamentation event seems to be the only responsible for 537
 transport of material outside of the eddy, since the rest of the 538
 particles remained inside the eddy boundaries. To get a rough 539
 estimate of the amount of matter expelled in the filamentation 540
 process we tracked the percentage of particles leaving a circle 541
 of diameter 200 km centered on the eddy center. In Fig. 11 542
 the time evolution of this percentage is shown for the particle 543
 sets released at different depths. The onset of filamentation is 544
 clearly visible around days 9-12 as a sudden increase in the per-

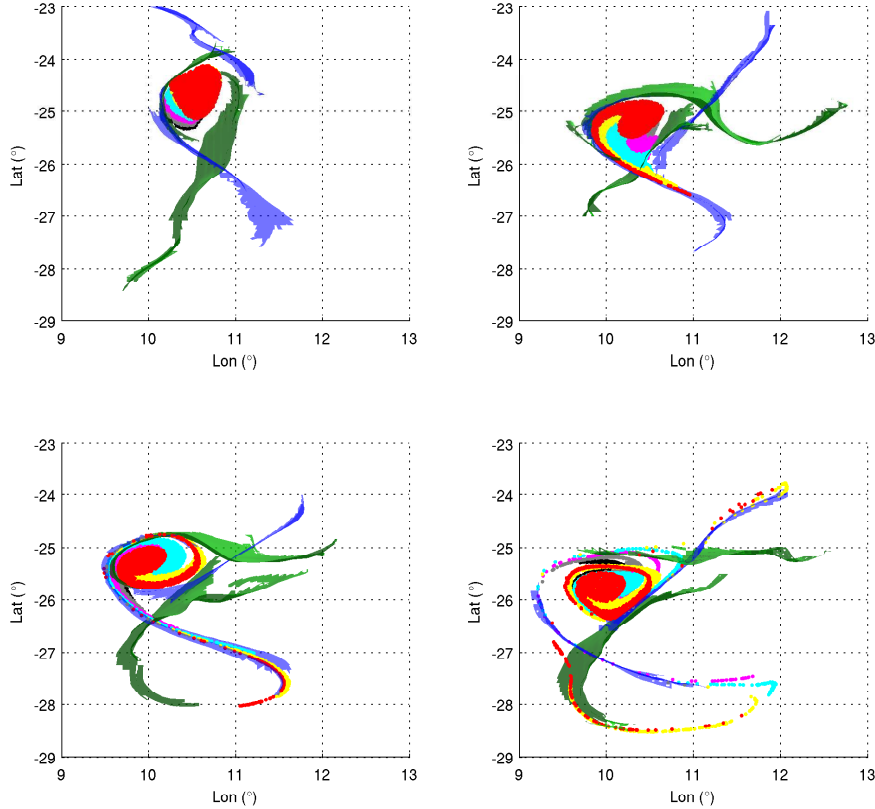


Figure 9: Top view of the evolution of particle patches and LCSs shown in Fig. 8. Top left: day 3; Top right: day 13; Bottom left: day 19; Bottom right: day 29. Colors as in figure 8.

545 centage of particles leaving the eddy. The percentage is maxi- 566
 546 mum for the particles located at 100 m depth and decreases as 567
 547 the depth increases. At 400 and 500 m depth there are no parti- 568
 548 cles leaving the circle. There is a clear lag between the onset of 569
 549 filamentation between the different depths: the onset is simulta- 570
 550 neous for the 40 m and 100 m depths but occurs later for larger 571
 551 depths.

552 4. Discussion.

553 The spatial average of FSLEs defines a measure of stirring 576
 554 and thus of horizontal mixing between the scales used for its 577
 555 computation. The larger the average, the larger the mixing activ- 578
 556 ity (d’Ovidio et al., 2004). The general trend in the verti- 579
 557 cal profiles of the average FSLE (Fig. 3) shows a reduction of 580
 558 mesoscale mixing with depth. There is however a rather inter- 581
 559 esting peak in this average profile occurring at 100 m, i.e. close 582
 560 to the thermocline. It could be related to submesoscale pro- 583
 561 cesses that occur alongside the mesoscale ones. Submesoscale 584
 562 is associated to filamentation (the thickness of filaments is of 585
 563 the order of 10 km or less), and we have seen that the filamen- 586
 564 tation and the associated transport intensity (Fig. 11) is higher 587
 565 at 100 m depth. It is not clear at the moment what is the precise 588

mechanism responsible for this increased activity at around 100 566
 567 m depth (perhaps associated to instabilities in the mixed layer), 568
 569 but we note that the intensity of shearing motions (see the Q 570
 571 plots in 5) is higher in the top 200 meters. Less intense filamen-
 572 tation could be caused by reduction of shear in depths larger
 573 than these values.

572 From an Eulerian perspective, it is thought that vortex fil-
 573 amentation occurs when the potential vorticity (PV) gradient
 574 aligns itself with the compressional axis of the velocity field,
 575 in strain coordinates (Louazel and Hua (2004);Lapeyre et al.
 (1999)). This alignment is accompanied by exponential growth
 of the PV gradient magnitude. The fact that the filamentation
 occurs along the attracting LCS seems to indicate that this ex-
 ponential growth of the PV gradient magnitude occurs across
 the attracting LCS.

582 In the specific spatiotemporal area we have studied, and in
 583 particular, for the eddy on which we focussed our analysis, we
 584 have confirmed that the structure of the LCSs is “curtain-like”,
 585 so that the strongest attracting and repelling structures are qua-
 586 sivertical surfaces. Their vertical extension would depend of the
 587 physical transport properties, but it is also altered by the partic-
 588 ular threshold parameter selected to extract the LCSs. These
 observations imply that transport and stirring occurs mainly on

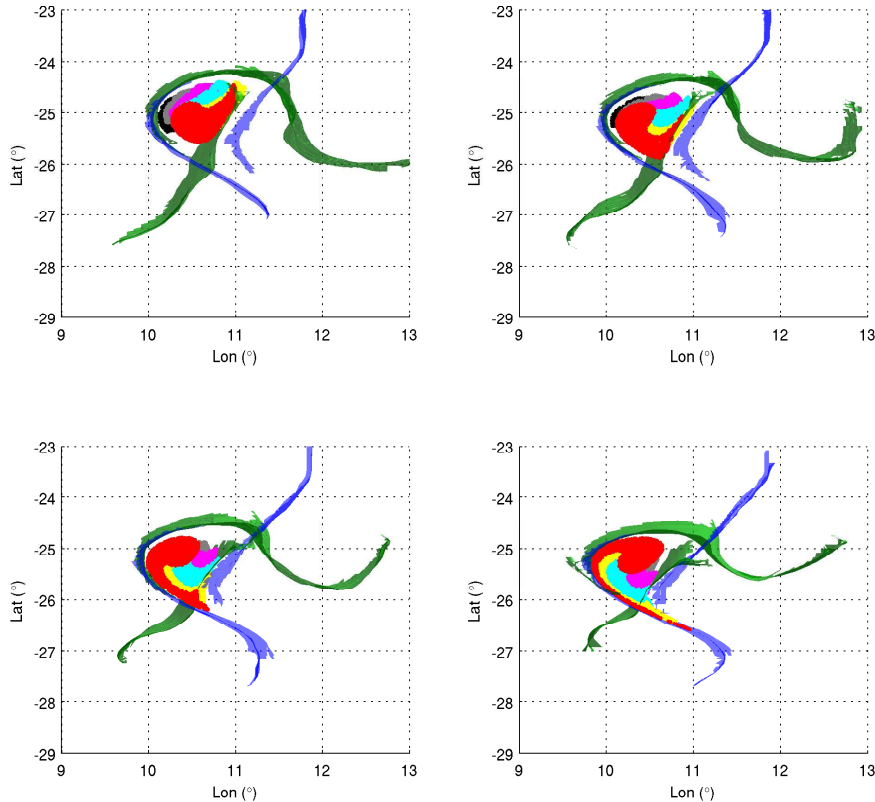


Figure 10: Top view of the initial stages of evolution of the particle patches and LCSs of Figs. 8 and 9. Top left: day 7; Top right: day 9; Bottom left: day 11; Bottom right: day 13. Colors as in figure 8.

589 the horizontal, which is a reasonable result considering the disparity 612
 590 between horizontal and vertical velocities in the ocean, 613
 591 and its stratification. However, we should mention that our results 614
 592 are not fully generalizable to all ocean situations, and that 615
 593 any ocean area or oceanic event should be studied in particular 616
 594 to reveal the shape of the associated 3d LCS.

595 Some comments follow about the nature of vertical transport 618
 596 structures. FSLEs are suited to the identification of hyperbolic 619
 597 structures (structures that exhibit high rates of transversal 620
 598 stretching or compression in their vicinity). The question is 621
 599 if one can expect that structures responsible for vertical transport 622
 600 will also exhibit substantial (vertical) stretching. This is 623
 601 not so clear in the ocean for the reasons already indicated. If 624
 602 one considers the case (relevant to our work) of purely isopycnal 625
 603 flow, then strong vertical stretching would be associated with 626
 604 a rapid divergence of isopycnic surfaces. In the case of 627
 605 coastal upwelling, for instance, the lifted isopycnic surfaces 628
 606 move vertically in a coherent fashion, so one should not expect 629
 607 strong vertical divergence of particles flowing along neighbouring 630
 608 isopycnic surfaces. This is just an example of the fact that it 631
 609 is possible that coherent vertical motions do not imply the presence 632
 610 of hyperbolic coherent structures such as those the FSLE 633
 611 may indicate.

Another possible limitation worth mentioning is the velocity 612
 field resolution and its relation to the intensity of the vertical 613
 velocity. It is accepted that in fronts or in the eddy periphery, 614
 vertical velocities are significantly greater than, for instance, in 615
 the eddy interior. These zones of enhanced vertical transport 616
 correspond to submesoscale features that were not adequately 617
 captured in the velocity field used in this work due to its coarse 618
 resolution, since submesoscale studies usually have resolutions 619
 < 10 km (the literature on this subject is quite large, so we refer 620
 the reader to Klein and Lapeyre (2009) and Lévy (2008)). 621

In any case, a most important point for the LCS we have 622
 computed is that in 3d, as in 2d, they act as pathways and barriers 623
 to transport, so that they provide a skeleton organizing the 624
 transport processes. 625

5. Conclusions

626 Three dimensional Lagrangian Coherent Structures were 627
 used to study stirring processes leading to dispersion and mixing 628
 at the mesoscale in the Benguela ocean region. We have 629
 computed 3d Finite Size Lyapunov Exponent fields, and LCSs 630
 were identified with the ridges these fields. LCSs appear as 631
 quasivertical surfaces, so that horizontal cuts of the FSLE fields 632

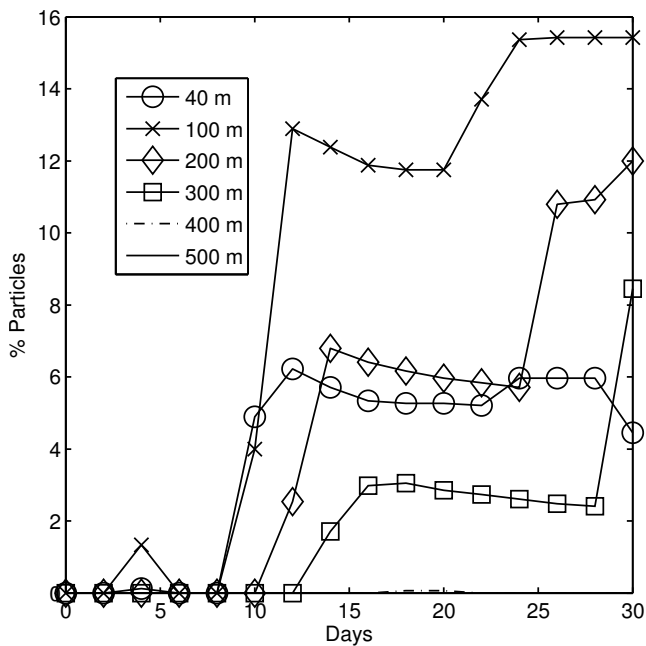


Figure 11: Percentage of particles outside a 200 km diameter circle centered at the eddy center, as a function of time.

gives already a quite accurate vision of the 3d FSLE distribution. These quasivertical surfaces appear to be coincident with the maximal lines of the FSLE field (see fig. 3) so that surface FSLE maps could be indicative of the position of 3d LCS, as long as the vertical shear of the velocity does not result in a significant deviation of the LCS with respect to the vertical. Average FSLE values generally decrease with depth, but we find a local maximum, and thus enhanced stretching and dispersion, at about 100 m depth.

We have also analyzed a prominent cyclonic eddy, pinched off the upwelling front and study the filamentation dynamics in 3d. Lagrangian boundaries of the eddy were made of intersections and tangencies of attracting and repelling LCS that apparently emanating from two hyperbolic locations North and South of the eddy. The LCS are seen to provide pathways and barriers organizing the transport processes and geometry. This pattern extends down up to the maximum depth were we calculated the FSLE fields (~ 600 m), but the exact shape of the boundary is difficult to determine due to the decrease in ridge strength with depth. This caused some parts of the LCS not to be extracted. The inclusion of a variable strength parameter in the extraction process is an important step to be included in the future.

The filamentation dynamics, and thus the transport out of the eddy, showed time lags with increasing depth. This arises from the vertical variation of the flow field. However the filamentation occurred along all depths, indicating that in reality vertical sheets of material are expelled from these eddies.

Many more additional studies are needed to further clarify the details of the geometry of the LCSs, their relationships with finite-time hyperbolic manifolds and three dimensional lobe dynamics, and specially their interplay with mesoscale and sub-

mesoscale transport and mixing processes.

Acknowledgements

Financial support from Spanish MICINN and FEDER through project FISICOS (FIS2007-60327) and from CSIC Intramural project TurBiD is acknowledged. JHB acknowledges financial support of the Portuguese FCT (Foundation for Science and Technology) through the predoctoral grant SFRH/BD/63840/2009. We thank the LEGOS group for providing us with 3D outputs of the velocity fields from their coupled BIOBUS/ROMS climatological simulation. The ridge extraction algorithm of Schultz et al. (2010) is available in the seek module of the data visualization library Teem (<http://teem.sf.net>).

References

- Amante, C., Eakins, B.W., 2009. ETOPO1 1 Arc-Minute Global Relief Model: Procedures, Data Sources and Analysis. NOAA Technical Memorandum NESDIS NGDC-24.
- Artale, V., Boffetta, G., Celani, A., Cencini, M., Vulpiani, A., 1997. Dispersion of passive tracers in closed basins: Beyond the diffusion coefficient. *Phys. Fluids* 9, 3162–3171.
- Aurell, E., Boffetta, G., Crisanti, A., Paladin, G., Vulpiani, A., 1997. Predictability in the large: an extension of the Lyapunov exponent. *J. Phys. A* 30, 1–26.
- Beron-Vera, F., Olascoaga, M., Goni, G., 2008. Oceanic mesoscale eddies as revealed by Lagrangian coherent structures. *Geophys. Res. Lett* 35, L12603.
- Boffetta, G., Lacorata, G., Redaelli, G., Vulpiani, A., 2001. Detecting barriers to transport: a review of different techniques. *Physica D* 159, 58–70.
- Branicki, M., Kirwan, A., 2010. Stirring: The Eckart paradigm revisited. *Int. J. Eng. Sci.* 48, 1027–1042.
- Branicki, M., Malek-Madani, R., 2010. Lagrangian structure of flows in the Chesapeake Bay: challenges and perspectives on the analysis of estuarine flows. *Nonlinear Processes in Geophysics* 17, 149–168.
- Branicki, M., Mancho, A.M., Wiggins, S., 2011. A Lagrangian description of transport associated with a front-eddy interaction: Application to data from the North-Western Mediterranean sea. *Physica D: Nonlinear Phenomena* 240, 282 – 304.
- Branicki, M., Wiggins, S., 2009. Finite-time Lagrangian transport analysis: Stable and unstable manifolds of hyperbolic trajectories and finite-time Lyapunov exponents. *Nonlinear Processes in Geophysics* 17, 1–36.
- Byrne, D.A., Gordon, A.L., Haxby, W.F., 1995. Agulhas eddies: A synoptic view using Geosat ERM data. *J. Phys. Oceanogr.* 25, 902–917.
- Doglioli, A., Blanke, B., Speich, S., Lapeyre, G., 2007. Tracking coherent structures in a regional ocean model with wavelet analysis: Application to cape basin eddies. *Journal of Geophysical Research C: Oceans* 112, C05043.
- d’Ovidio, F., Fernández, V., Hernández-García, E., López, C., 2004. Mixing structures in the Mediterranean sea from Finite-Size Lyapunov Exponents. *Geophys. Res. Lett.* 31, L17203.
- d’Ovidio, F., Isern, J., López, C., Hernández-García, E., García-Ladona, E., 2009. Comparison between Eulerian diagnostics and Finite-Size Lyapunov Exponents computed from Altimetry in the Algerian basin. *Deep-Sea Res.* I 56, 15–31.
- Eberly, D., Gardner, R., Morse, B., Pizer, S., Scharlach, C., 1994. Ridges for image analysis. *Journal of Mathematical Imaging and Vision* 4, 353–373.
- Elhmaili, D., Provenzale, A., Babiano, A., 1993. Elementary topology of two-dimensional turbulence from a Lagrangian viewpoint and single-particle dispersion. *J. Fluid Mech.* 257, 533–558.
- Haller, G., 2000. Finding finite-time invariant manifolds in two-dimensional velocity fields. *Chaos* 10(1), 99–108.
- Haller, G., 2001. Distinguished material surfaces and coherent structure in three-dimensional fluid flows. *Physica D* 149, 248–277.
- Haller, G., 2002. Lagrangian coherent structures from approximate velocity data. *Phys. Fluids A* 14, 1851–1861.

- Haller, G., 2011. A variational theory of hyperbolic lagrangian coherent structures. *Physica D* 240, 574–598.
- Haller, G., Yuan, G., 2000. Lagrangian coherent structures and mixing in two-dimensional turbulence. *Physica D* 147, 352–370.
- Haza, A., Özgökmen, T., Griffa, A., Molcard, A., Poulain, P.M., Peggion, G., 2010. Transport properties in small-scale coastal flows: relative dispersion from VHF radar measurements in the Gulf of La Spezia. *Ocean Dynamics* 60, 861–882.
- Haza, A.C., Poje, A.C., Özgökmen, T.M., Martin, P., 2008. Relative dispersion from a high-resolution coastal model of the Adriatic Sea. *Ocean Modell.* 22, 48–65.
- Hernandez-Carrasco, I., López, C., Hernández-García, E., Turiel, A., 2011. How reliable are finite-size Lyapunov exponents for the assessment of ocean dynamics? *Ocean Modell.* 36, 208–218.
- Hunt, J.C.R., Wray, A.A., Moin, P., 1988. Eddies, Streams and Convergence Zones in Turbulent Flows. Technical Report CTR-S88. Center for Turbulence Research, Stanford University. 193–208.
- Jeong, J., Hussain, F., 1995. On the identification of a vortex. *J. Fluid Mech.* 285, 69–94.
- Joseph, B., Legras, B., 2002. Relation between kinematic boundaries, stirring, and barriers for the Antarctic polar vortex. *J. Atm. Sci.* 59, 1198–1212.
- Klein, P., Lapeyre, G., 2009. The oceanic vertical pump induced by mesoscale and submesoscale turbulence. *Ann. Rev. Mar. Sci.* 1, 351–375.
- Lacasse, J., 2008. Statistics from Lagrangian observations. *Progress in oceanography* 77, 1–29.
- Lapeyre, G., Klein, P., Hua, B., 1999. Does the tracer gradient vector align with strain eigenvectors in 2d turbulence? *Phys. Fluids* 11, 3729–3737.
- Le Vu, B., Gutknecht, E., Machu, E., Dadou, I., Veitch, J., Sudre, J., Paulmier, A., Garçon, V., 2011. Processes maintaining the OMZ of the Benguela upwelling system using an eddy resolving model. submitted to *JMR*.
- Lehahn, Y., d’Ovidio, F., Lévy, M., Amitai, Y., Heifetz, E., 2011. Long range transport of a quasi isolated chlorophyll patch by an Agulhas ring. *Geophys. Res. Lett.* 38, L16610.
- Lekien, F., Shadden, S.C., Marsden, J.E., 2007. Lagrangian coherent structures in n-dimensional systems. *J. Math. Phys.* 48, 065404.
- Louazel, S., Hua, B.L., 2004. Vortex erosion in a shallow-water model. *Physics of Fluids* 16, 3079–3085.
- Lévy, M., 2008. The modulation of biological production by oceanic mesoscale turbulence, in: Weiss, J., Provenzale, A. (Eds.), *Transport and Mixing in Geophysical Flows*. Springer Berlin / Heidelberg. volume 744 of *Lecture Notes in Physics*, pp. 219–261.
- Mahadevan, A., 2006. Modeling vertical motion at ocean fronts: Are nonhydrostatic effects relevant at submesoscales? *Ocean Modelling* 14, 222 – 240.
- Mancho, A.M., Small, D., Wiggins, S., 2006. A tutorial on dynamical systems concepts applied to Lagrangian transport in ocean flows defined as finite time data sets: theoretical and computational issues. *Phys. Rep.* 437, 55–124.
- Mariano, A.J., Griffa, A., Özgökmen, T., Zambianchi, E., 2002. Lagrangian analysis and predictability of coastal and ocean dynamics 2000. *J. Atmos. Oceanic Technol.* 19, 1114–1126.
- McGillicuddy, D.J., Robinson, A.R., Siegel, D.A., Jannasch, H.W., Johnson, R., Dickey, T.D., McNeil, J., Michaels, A.F., Knap, A.H., 1998. Influence of mesoscale eddies on new production in the Sargasso sea. *Nature* 394, 263–266.
- Molcard, A., Poje, A., Özgökmen, T., 2006. Directed drifter launch strategies for Lagrangian data assimilation using hyperbolic trajectories. *Ocean Modell.* 12, 268–289.
- Okubo, A., 1970. Horizontal dispersion of floatable particles in the vicinity of velocity singularities such as convergences. *Deep-Sea Res.* 17, 445–454.
- Oschlies, A., Garçon, V., 1998. Eddy-induced enhancement of primary productivity in a model of the North Atlantic ocean. *Nature* 394, 266–269.
- Özgökmen, T.M., Poje, A.C., Fischer, P.F., Haza, A.C., 2011. Large eddy simulations of mixed layer instabilities and sampling strategies. *Ocean Modell.* 39, 311–331.
- Pauly, D., Christensen, V., 1995. Primary production required to sustain global fisheries 374, 255–257.
- Poje, A.C., Haza, A.C., Özgökmen, T.M., Magaldi, M.G., Garraffo, Z.D., 2010. Resolution dependent relative dispersion statistics in a hierarchy of ocean models. *Ocean Modell.* 31, 36–50.
- Pouransari, Z., Speetjens, M., Clercx, H., 2010. Formation of coherent structures by fluid inertia in three-dimensional laminar flows. *J. Fluid Mech.* 654, 5–34.
- Provenzale, A., 1999. Transport by coherent barotropic vortices. *Annu. Rev. Fluid Mech.* 31, 55–93.
- Rossi, V., López, C., Sudre, J., Hernández-García, E., Garçon, V., 2008. Comparative study of mixing and biological activity of the Benguela and Canary upwelling systems. *Geophys. Res. Lett.* 35, L11602.
- Rubio, A., Blanke, B., Speich, S., Grima, N., Roy, C., 2009. Mesoscale eddy activity in the southern Benguela upwelling system from satellite altimetry and model data. *Progress In Oceanography* 83, 288 – 295.
- Sadlo, F., Peikert, R., 2007. Efficient visualization of Lagrangian Coherent Structures by filtered AMR ridge extraction. *IEEE Transactions on Visualization and Computer Graphics* 13, 1456–1463.
- Schultz, T., Theisel, H., Seidel, H.P., 2010. Crease surfaces: From theory to extraction and application to diffusion tensor MRI. *IEEE Transactions on Visualization and Computer Graphics* 16, 109–119.
- Shadden, S.C., Lekien, F., Marsden, J.E., 2005. Definition and properties of Lagrangian coherent structures from finite-time Lyapunov exponents in two-dimensional aperiodic flows. *Physica D.* 212, 271–304.
- Shchepetkin, A.F., McWilliams, J.C., 2003. A method for computing horizontal pressure-gradient force in an oceanic model with a nonaligned vertical coordinate. *J. Geophys. Res.* 108, 3090.
- Shchepetkin, A.F., McWilliams, J.C., 2005. The regional ocean modeling system: A split-explicit, free-surface, topography following coordinates ocean model. *Ocean Modell.* 9, 347–404.
- Tallapragada, P., Ross, S.D., Schmale III, D.G., 2011. Lagrangian coherent structures are associated with fluctuations in airborne microbial populations. *Chaos* 21, 033122.
- Tang, W., Chan, P.W., Haller, G., 2011. Lagrangian coherent structure analysis of terminal winds detected by lidar. part I: Turbulence structures. *Journal of Applied Meteorology and Climatology* 50, 325–338.
- Thomas, L., Tandon, A., Mahadevan, A., 2008. Submesoscale ocean processes and dynamics, in: Hecht, M., Hasume, H. (Eds.), *Ocean Modeling in an Eddying Regime*, Geophysical Monograph 177, American Geophysical Union, Washington D.C., pp. 17–38.
- du Toit, P., Marsden, J., 2010. Horseshoes in hurricanes. *Journal of Fixed Point Theory and Applications* 7, 351–384. 10.1007/s11784-010-0028-6.
- Waugh, D.W., Abraham, E.R., Bowen, M.M., 2006. Spatial variations of stirring in the surface ocean: A case of study of the Tasman sea. *J. Phys. Oceanogr.* 36, 526–542.
- Weiss, J., 1991. The dynamics of enstrophy transfer in two-dimensional hydrodynamics. *Physica D* 48, 273–294.
- Yuan, K.Y., Huang, Y.S., Yang, H.T., Pian, T.H.H., 1994. The inverse mapping and distortion measures for 8-node hexahedral isoparametric elements. *Computational Mechanics* 14, 189–199.